Hindawi
Mathematical Problems in Engineering
Volume 2019, Article ID 1264715, 10 pages
https://doi.org/10.1155/2019/1264715

Research Article

A Novel Designed Sparse Array for Noncircular Sources with High Degree of Freedom

Yan-kui Zhang,[1] Hai-yun Xu ,[1] Da-ming Wang,[1] Bin Ba ,[1] and Si-yao Li[2]

[1]*National Digital Switching System Engineering and Technology Research Center, Zhengzhou 450002, China*
[2]*Communication NCO Academy, Army Engineering University, Nanjing 210000, China*

Correspondence should be addressed to Hai-yun Xu; xuhaiyun1995@163.com

Received 1 September 2018; Revised 8 December 2018; Accepted 26 December 2018; Published 29 January 2019

Academic Editor: Raffaele Solimene

The existing coprime array is mainly applicable to circular sources, while the virtual array degree of freedom (DOF) for noncircular sources is enhanced limitedly. In order to perfect the array DOF and the direction of arrival (DOA) estimation accuracy, a high degree of freedom sparse array design method for noncircular sources is put forward. Firstly, the method takes the advantages of the characteristic of the noncircular sources to expand the array manifold and then explores and solves the location distribution of the physical array sensors on the basis of the virtual array model with the help of the searching approach. The array configuration can obtain the longest continuous virtual array. The comparisons between the proposed array configuration and the common array configurations are advanced. The simulation experiments show that the sparse array presented in this paper can effectively increase the continuous virtual array aperture of noncircular sources, improve the array DOF and DOA estimation accuracy, and achieve the purpose of better estimation of multiple DOAs in underdetermined conditions.

1. Introduction

Direction of arrival (DOA) estimation is one of the main research topics in array signal processing. It is widely used in radar, sonar, radio astronomy, and so on [1, 2]. The traditional DOA estimation algorithms are mainly based on the uniform array, and the M array sensors can achieve at most $M - 1$ effective estimation of the azimuths [3, 4]. The number of target sources needed to be located is sometimes greater than the number of array sensors, that is, underdetermined condition. In order to improve the array degree of freedom (DOF) and realize the effective estimation of multiple sources in undetermined condition, in recent years, many sparse array structures have been proposed by experts and scholars. With the new sparse arrays, the apertures of arrays can be effectively extended, and the array DOFs and estimation accuracy could be improved [5, 6].

Typical sparse arrays include the minimum redundancy array (MRA), the minimum hole array (MHA), the nested array, and the coprime array [7]. MRAs and MHAs are the ideal array configurations for circular sources; the optimal virtual array can be achieved [8, 9]. The nested array consists of a nonsparse uniform array and a sparse uniform array, which ensures a higher array DOF and continuous virtual array [10, 11]. The coprime array is composed of two uniform sparse arrays with larger array sensor spacing and a high array DOF, and the nested array is a special type of coprime array [12, 13]. The general structure of the coprime array and the solutions to basic DOA estimation are given in [14, 15]. The authors of [16, 17] propose improved coprime arrays and use the spatial smoothing algorithm for the virtual array to improve the estimation precision. In [18, 19], a coprime array with displaced subarrays (CADiS) structure is exploited. This coprime array configuration greatly expands the array aperture, improves the array DOF, and increases estimation accuracy. On the basis of the CADiS configuration, [20] summarizes the general configuration of coprime array with multiperiod subarrays (CAMpS) and proves that the CADiS is a special form of CAMpS. A kind of shifted coprime array (SCA) is proposed in [21], which further improves the virtual array aperture of CADiS configuration. The sparse array configurations mentioned above are mainly focused on the DOA estimation of circular sources, and there is no open research on the sparse configurations designed for noncircular sources.

A noncircular source is a special transmission signal. Compared with a circular source, a noncircular source has more useful information. One of the most important features is that the ellipse covariance of noncircular sources is not zero. Therefore, this characteristic can be used to improve the array DOF and the DOA estimation accuracy. A DOA estimation method based on symmetric shift invariance array for noncircular sources is presented in [22], which enhances the array DOF by using the noncircular characteristic. Some DOA estimation methods for noncircular sources are listed in document [23–27]. These methods extend the array aperture by using the noncircular characteristics of sources and advance the array DOF and estimation accuracy.

The DOA estimation methods mentioned above for the noncircular sources are all based on the array configuration of circular sources, and the array DOF and estimation accuracy are improved by using the characteristic that the ellipse covariance is not zero, but the use of this characteristic is not sufficient. In order to further increase the array DOF of noncircular sources and improve the accuracy of DOA estimation, a novel high DOF sparse array design approach for noncircular sources is presented in this paper. In this configuration, the virtual array model is constructed by using the characteristics of noncircular sources. Then the maximum continuous virtual array structure of noncircular sources is given by search method on the basis of difference. At last, the typical DOA estimation methods under this model are given. The validity of the method is proven by simulation experiments.

The main contributions of this paper are as follows.

(1) A novel designed sparse array for noncircular sources (SANC) with high DOF is proposed, which effectively extends the continuous virtual array aperture and improves the DOA estimation accuracy.

(2) The design method and flow chart of the SANC configuration are given in this paper. The comparison between the array configuration proposed and the common array configurations is given, and typical DOA estimation methods under this array configurations are introduced.

(3) A virtual array model is constructed, and the Cramer-Rao lower bound (CRLB) is derived under the proposed model, effectively proving that the proposed array configuration not only can realize the effective estimation in overdetermined conditions but also is suitable for underdetermined conditions.

The remainder of this paper is arranged as follows. Section 2 introduces the typical coprime array model. Section 3 describes the SANC configuration. The typical DOA estimation methods under this array configuration are given in Section 4. The performance analysis and simulation experiments are presented in Section 5. Section 6 is the conclusion of this paper.

2. Coprime Array Model

2.1. Notation Conventions. Notations used in this paper are as follows:

(i) $\mathbf{I}_N$ represents N-dimensional unit array.

(ii) $(\cdot)^*$, $(\cdot)^{\mathrm{T}}$, and $(\cdot)^{\mathrm{H}}$, respectively, represent conjugate, transposition, and conjugate transpose.

(iii) $[\cdot]_m$ stands for the mth element of this vector.

(iv) $\odot$ represents Hadamard product.

(v) $\bigcup$ stands for the intersection.

(vi) $vec[\cdot]$ is the operation of "vectorization," which means turning a matrix into a vector by columns.

(vii) $\otimes$ is the Kronecker product.

(viii) $E(\cdot)$ denotes the mathematical expectation.

(ix) $\|\cdot\|_0$, $\|\cdot\|_1$, and $\|\cdot\|_2^2$, respectively, represent the 0-norm, 1-norm, and 2-norm.

(x) Re$[\cdot]$ and Im$[\cdot]$ denotes the real part and the imaginary part.

2.2. Coprime Array Model. We assume that there are D stationary narrowband targets transmitting plane waves to the measuring array. The direction-of-arrivals is $\theta = (\theta_1, \theta_2, \cdots \theta_D)$ and the corresponding source powers are $\mathbf{p} = (\sigma_1^2, \sigma_2^2, \cdots \sigma_D^2)$. The measuring array is a linear array with M sensors. k is the snapshot index, $k \in \{1, 2 \cdots K\}$; the kth receiving snapshot can be expressed as

$$\mathbf{x}(k) = \sum_{i=1}^{D} \mathbf{a}(\theta_i)\, \mathbf{s}_i(k) = \mathbf{A}\mathbf{s}(k) + \mathbf{n}(k) \tag{1}$$

where $\mathbf{x}(k)$ is the receiving signal vector, $\mathbf{s}(k)$ is the transmission signal vector, $\mathbf{A}$ is the array manifold, $\mathbf{n}(k)$ is the additive Gaussian white noise vector with a power of σ_n^2, and $\mathbf{a}(\theta_i)$ is the steering vector:

$$\mathbf{a}(\theta_i) = \left(1, e^{-j2\pi(d_1 \sin\theta_i/\lambda)}, e^{-j2\pi(d_2 \sin\theta_i/\lambda)}, \cdots e^{-j2\pi(d_{M-1} \sin\theta_i/\lambda)}\right)^{\mathrm{T}} \tag{2}$$

d_m represents the distance between the mth antenna and the first antenna in the array configuration, $d_m \in \mathbb{P}$, where $\mathbb{P}$ is the location set of the physical sensors. If the array is a coprime array, then

$$d_m \in \{0, M_1 d \cdots M_1(M_2 - 1)d\} \bigcup \{M_2 d \cdots M_2(M_1 - 1)d\} \tag{3}$$

The geometric configuration of the coprime array is shown in Figure 1, where d is the fundamental sensor spacing, $d = \lambda/2$, and λ is the wavelength of the transmitting signal. M_1 and M_2 are coprime integers, and $M = M_1 + M_2 - 1$ is the total number of sensors. The covariance matrix of the received signal is expressed as

$$\mathbf{R}_{\mathbf{XX}} = \mathrm{E}\left[\mathbf{x}(k)\,\mathbf{x}(k)^{\mathrm{H}}\right] = \sum_{i=1}^{D} \sigma_i^2 \mathbf{a}(\theta_i)\,\mathbf{a}(\theta_i)^{\mathrm{H}} + \sigma_n^2 \mathbf{I} = \mathbf{A}\mathbf{R}_{ss}\mathbf{A}^{\mathrm{H}} + \sigma_n^2 \mathbf{I} \tag{4}$$

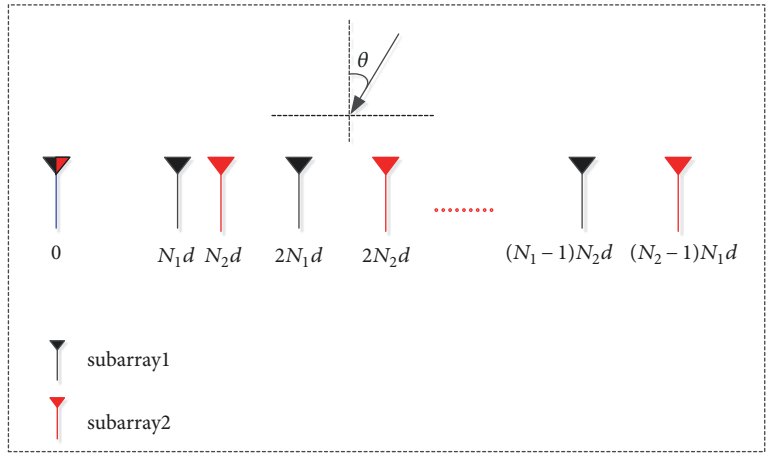

Figure 1: Geometry of coprime array.

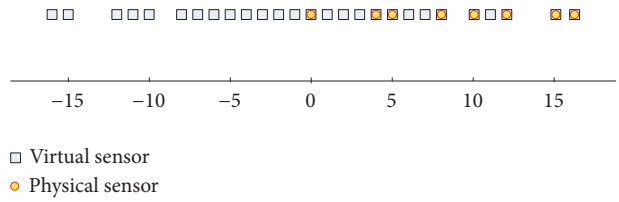

Figure 2: Position distribution of the physical array and virtual array ($M_1 = 4$ and $M_2 = 5$).

$\mathbf{R}_{ss}$ is the covariance matrix of the transmitted signal. In practice, the statistical mean is used to replace the mathematical mean; that is,

$$\mathbf{R}_{\mathbf{XX}} = \frac{1}{K}\sum_{k=1}^{K}\mathbf{x}(k)\,\mathbf{x}(k)^{\mathrm{H}} \tag{5}$$

$E[x_u(k)x_v^*(k)]$ is the uth line and vth column of the covariance matrix $\mathbf{R}_{\mathbf{XX}}$, which can be expressed as

$$R_{u,v} = e^{-j2\pi(\sin\theta_i/\lambda)(d_u - d_v)}\sigma_i^2 \tag{6}$$

where $d_u \in \mathbb{P}$ and $d_v \in \mathbb{P}$. We define the difference set as

$$\mathbb{D} = \{d_u - d_u \mid 0 \le u,\ v \le M-1\} \tag{7}$$

The difference set is the basis of the virtual array, and the elements in the difference set represent the relative position of the virtual array. The location distribution of the physical elements and the virtual array are shown in Figure 2 for $M_1 = 4$ and $M_2 = 5$. Obviously, the independent difference is symmetric on the center of origin.

3. Sparse Array for Noncircular Sources (SANC) with High Degree of Freedom

3.1. SANC Configuration Design. The circular sources are the universal assumption of narrow band sources. Its definition comes from the first- and second-order statistical characteristics of the sources. When the ellipse covariance of the sources is zero, the sources are called circular sources. When the ellipse covariance is not zero, the sources are noncircular sources, and the common noncircular sources are BPSK, AM, ASK, and PAM. The constellation diagram of circular sources consists of in-phase components and quadrature components. Compared with circular sources, noncircular sources have more useful information, so the DOA estimation accuracy of noncircular sources can be improved by using this characteristic.

A notable feature of noncircular sources is that the elliptical covariance of sources is not zero.

$$\mathbf{R}'_{\mathbf{XX}} = \mathrm{E}\left[\mathbf{x}(k)\,\mathbf{x}(k)^{\mathrm{T}}\right] \neq \mathbf{0} \tag{8}$$

With the noncircular characteristics of the sources, the aperture of the array can be expanded.

$$\mathbf{y}(k) = \begin{bmatrix}\mathbf{x}(k)\\ \mathbf{x}^*(k)\end{bmatrix} = \begin{bmatrix}\mathbf{A}\\ \mathbf{A}^*\end{bmatrix}\mathbf{s}(k) + \begin{bmatrix}\mathbf{n}(k)\\ \mathbf{n}^*(k)\end{bmatrix} \tag{9}$$

The equivalent array manifold is $\mathbf{B} = \left[\begin{smallmatrix}\mathbf{A}\\ \mathbf{A}^*\end{smallmatrix}\right] = [\mathbf{b}(\theta_1)\cdots, \mathbf{b}(\theta_D)]$; $\mathbf{b}(\theta_i) = \left[\begin{smallmatrix}\mathbf{a}(\theta_i)\\ \mathbf{a}^*(\theta_i)\end{smallmatrix}\right]$; and the extended covariance matrix is

$$\begin{aligned}\mathbf{R}_{\mathbf{yy}} &= \mathrm{E}\left[\mathbf{y}(k)\,\mathbf{y}(k)^{\mathrm{H}}\right] = \sum_{i=1}^{D}\sigma_i^2\mathbf{b}(\theta_i)\,\mathbf{b}(\theta_i)^{\mathrm{H}} + \sigma_n^2\mathbf{I}\\ &= \mathbf{B}\mathbf{R}_{ss}\mathbf{B}^{\mathrm{H}} + \sigma_n^2\mathbf{I}\end{aligned} \tag{10}$$

Because $\mathbf{b}(\theta_i)\mathbf{b}(\theta_i)^{\mathrm{H}}$ extends the virtual array aperture, according to formula (6), the virtual array manifold of the

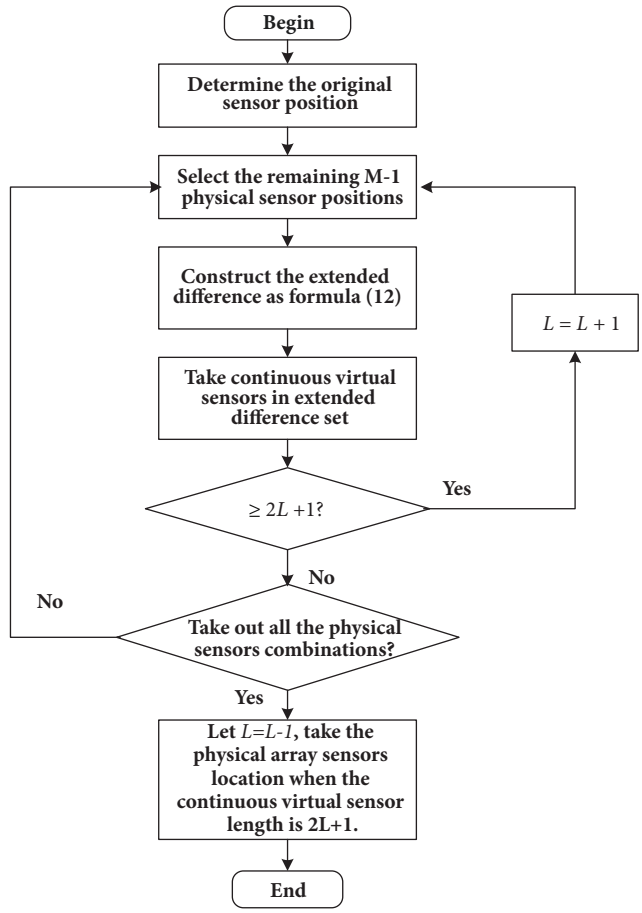

Figure 3: Flow chart of the design method for SANC configuration.

extended array for noncircular sources can be obtained; that is,

$$\mathbb{D}_{\mathrm{NC}} = \{d_u - d_v, d_u + d_v, -d_u - d_v \mid 0 \le u, v \le M-1\} \tag{11}$$

Generally, to achieve the maximum array DOF with the spatial smoothing method, the virtual array aperture needs to reach the maximum; that is, the number of continuous virtual array sensors reaches the maximum. In order to achieve the maximum number of continuous virtual array sensors, exhaustion method is used to search the optimal distribution of physical sensors. The search steps are divided into four steps as follows.

Step 1. Based on the number of physical elements M, we set the number of continuous virtual array sensors $2L + 1$; that is, the virtual array sensors are continuous in the range $[-L, L]$, because the virtual array is symmetry about origin of coordinates, so the distribution range of the physical sensor is set $[0, 2L]$ (the physical array sensor distribution can also be taken in a wider range, but the search is more complex), the position of the first physical element is 0, and take arbitrary $M - 1$ physical positions in the range $[1, 2L]$.

Step 2. According to the physical sensors position taken in Step 1, the extended difference set of the noncircular sources is constructed by formula (11). If the number of continuous virtual elements is less than $2L + 1$, the Step 1 is repeated. If all the possible physical array sensors are taken out and the length of the continuous virtual array sensors is all less than $2L + 1$, then Step 4 is executed; if there is a physical array distribution, which makes the number of continuous virtual elements greater than or equal to $2L + 1$, then perform Step 3.

Step 3. Let $L = L + 1$; return to execute Step 1.

Step 4. Let $L = L - 1$; the position distribution of the physical sensors is obtained when the continuous virtual array length is equal to $2L + 1$ in Step 2, which is the optimal physical sensors distribution of SANC. The flow chart of this method is shown in Figure 3.

3.2. Comparison of Different Array Structures. The SANC with high DOF is designed to increase the continuous virtual aperture effectively. In order to show the aperture advantage of the proposed array configuration, this section firstly gives the physical sensors distribution of SANC when the number of array elements is 2 to 10, as shown in Table 1.

Table 1: The physical array sensors distribution of SANC.

M	$\{d_i\}$	$2L+1$
2	{0, 1}	5
3	{0, 2, 3}	13
4	{0, 2, 4, 5}	21
5	{0, 1, 2, 8, 13}	33
6	{0, 4, 8, 10, 11, 13}	49
7	{0, 5, 7, 12, 13, 15, 16}	65
8	{0, 6, 12, 15, 16, 17, 19, 20}	81
9	{0, 6, 12, 18, 21, 22, 23, 25, 26}	105
10	{0, 6, 12, 18, 24, 27, 28, 29, 31, 32}	129

Table 2: Comparison of maximum continuous virtual array aperture and DOF for typical array configurations.

Array configurations	$\{d_i\}$	$2L+1$	DOF
Uniform array	0, 1, 2, 3, 4, 5, 6, 7	29	15
Nest array	0, 1, 2, 3, 4, 8, 12, 16	41	21
Coprime array	0, 4, 5, 8, 10, 12, 15, 16	57	29
Nested CADiS	0, 1, 2, 3, 8, 12, 16, 20	49	25
MRA	0, 1, 2, 5, 8, 11, 12, 13	53	27
Proposed (SANC)	0, 6, 12, 15, 16, 17, 19, 20	81	41

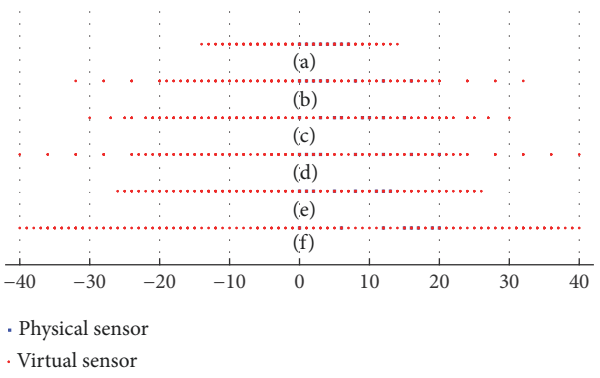

Figure 4: Distribution of the physical sensors and the virtual elements of typical array configurations: (a) uniform array, (b) nested array, (c) coprime array, (d) nested CADiS array, (e) MRA, and (f) SANC array.

The distribution of physical sensors and virtual array sensors of SANC and five typical sparse arrays with 8 array elements are shown in Figure 4. To fully exploit the advantages of the CADiS array, the nested CADiS is used in the comparison. In the comparison, the distribution of physical array sensors is {0, 6, 12, 15, 16, 17, 19, 20}. From Figure 4, we can see that the virtual aperture of the proposed array is the largest and the number of continuous virtual sensors is the largest. To clearly present the structural advantages of SANC, Table 2 lists the maximum number of continuous virtual array elements and the DOF for the case of a physical array of 8 sensors; the DOF here is an example for space smoothing algorithm. According to the data comparison in Table 2, the proposed array configuration effectively improves the aperture of the virtual array and increases the array DOF.

4. DOA Estimation Methods

There are many typical DOA estimation methods, such as subspace-based methods, compressed sensing methods, and high-order statistics methods. Here we briefly introduce the common subspace-based method and compressed sensing method.

4.1. Spatial Smoothing MUSIC Algorithm. In order to make full use of the maximum continuous virtual array of SANC above, the received source covariance matrix is vectorized as follows:

$$\begin{aligned}\mathbf{z} &= vec\left(\mathbf{R}_{yy}\right) = vec\left(\sum_{i=1}^{D}\sigma_i^2\mathbf{b}\left(\theta_i\right)\mathbf{b}\left(\theta_i\right)^{\mathrm{H}}\right) + \sigma_n^2\widetilde{\mathbf{I}} \\ &= \widetilde{\mathbf{B}}\left(\theta_1, \theta_2, \cdots \theta_D\right)\mathbf{p} + \sigma_n^2\widetilde{\mathbf{I}}\end{aligned} \tag{12}$$

where

$$\begin{aligned}\widetilde{\mathbf{B}}\left(\theta_1, \cdots \theta_D\right) = &\left[\mathbf{b}^*\left(\theta_1\right) \otimes \mathbf{b}\left(\theta_1\right), \mathbf{b}^*\left(\theta_2\right)\right. \\ &\left.\otimes \mathbf{b}\left(\theta_2\right), \cdots \mathbf{b}^*\left(\theta_D\right) \otimes \mathbf{b}\left(\theta_D\right)\right]\end{aligned} \tag{13}$$

$$\widetilde{\mathbf{I}} = vec\left(\mathbf{I}_{2M}\right) \tag{14}$$

$\widetilde{\mathbf{B}}$ is the extended virtual array manifold. If the length of the maximum continuous virtual array is $2L+1$, we take the maximum continuous virtual element response part in $\widetilde{\mathbf{B}}$ to reconstruct a $(2L+1) \times D$-dimensional uniform array. So

$$\widehat{\mathbf{z}} = \widehat{\mathbf{B}}\mathbf{p} + \sigma_n^2\widehat{\mathbf{I}} \tag{15}$$

We apply spatial smoothing to $\widehat{\mathbf{z}}$, where $\widehat{\mathbf{z}}$ has a conjugate symmetric distribution. Therefore, the length of the smooth

segment is $L+1$. The position of the ith smooth subarray is $\widehat{\mathbf{z}}_i$, and the noise vector is $\sigma_n^2\widehat{\mathbf{e}}_i$; for the virtual array,

$$\{(-i+1+n)\,d,\ n=0,1,\cdots,L\} \tag{16}$$

$$\widehat{\mathbf{z}}_i=\widehat{\mathbf{B}}_i\mathbf{p}+\sigma_n^2\widehat{\mathbf{I}}_i=\widehat{\mathbf{B}}_1\boldsymbol{\Phi}^{i-1}\mathbf{p}+\sigma_n^2\widehat{\mathbf{I}}_i \tag{17}$$

where

$$\boldsymbol{\Phi}=\begin{pmatrix} e^{-j\pi\sin\theta_1} & & & \\ & e^{-j\pi\sin\theta_2} & & \\ & & \ddots & \\ & & & e^{-j\pi\sin\theta_D} \end{pmatrix} \tag{18}$$

$$\widehat{\mathbf{B}}_1=\begin{pmatrix} 1 & 1 & \cdots & 1 \\ \widehat{b}(\theta_1) & \widehat{b}(\theta_2) & \cdots & \widehat{b}(\theta_D) \\ \vdots & \vdots & \vdots & \vdots \\ \widehat{b}(\theta_1)^L & \widehat{b}(\theta_2)^L & \cdots & \widehat{b}(\theta_D)^L \end{pmatrix} \tag{19}$$

$\widehat{\mathbf{b}}(\theta_i)=[1,\widehat{b}(\theta_i),\cdots,(\widehat{b}(\theta_i))^L]^{\mathrm{T}}$; $\widehat{b}(\theta_i)=e^{-j\pi\sin\theta_i}$. The weighted mean for all of the covariance matrices of the smooth subarray is

$$\mathbf{R}=\frac{1}{L+1}\sum_{i=1}^{L+1}\widehat{\mathbf{z}}_i\widehat{\mathbf{z}}_i^{\mathrm{H}} \tag{20}$$

Eigenvalue decomposition (EVD) is applied to $\mathbf{R}$ as follows:

$$\mathbf{R}=\mathbf{U}_s\boldsymbol{\Sigma}_s\mathbf{U}_s^{\mathrm{H}}+\mathbf{U}_n\boldsymbol{\Sigma}_n\mathbf{U}_n^{\mathrm{H}} \tag{21}$$

Because the signal subspace and the noise subspace are orthogonal, the steering vector and the signal subspace belong to the same vector space, so the spatial spectral expression of the DOAs is

$$\mathbf{P}=\frac{1}{\widehat{\mathbf{b}}^{\mathrm{H}}(\theta)\,\mathbf{U}_n\mathbf{U}_n^{\mathrm{H}}\widehat{\mathbf{b}}(\theta)} \tag{22}$$

The root-MUSIC method or spectral peak search method can be used to solve all the direction-of-arrivals.

4.2. Compressed Sensing Approach. Other typical DOA estimation methods are based on compressed sensing approaches. Since the DOAs fall on the finite discrete angles, the spatial signal spectra are sparse. Therefore, sparsity-based techniques can be applied to DOA estimation to improve the array DOF. There are many typical compressed sensing methods [28–30]; LASSO is one of the representative compressed sensing methods. Firstly, a complete set $\boldsymbol{\Pi}=\{\overline{\theta}_1,\overline{\theta}_2,\cdots\overline{\theta}_\Gamma\}$ is constructed, which is called a redundant dictionary. $\boldsymbol{\Pi}$ contains all the possible direction-of-arrivals, and $\Gamma\gg D$. Based on this, a compressed sensing model is build as follows:

$$\mathbf{z}=\widetilde{\mathbf{B}}\left(\overline{\theta}_1,\overline{\theta}_2,\cdots\overline{\theta}_\Gamma\right)\overline{\mathbf{p}}+\sigma_n^2\widetilde{\mathbf{I}} \tag{23}$$

$\widetilde{\mathbf{B}}(\overline{\theta}_1,\overline{\theta}_2,\cdots\overline{\theta}_\Gamma)$ is the sensing matrix; $\overline{\mathbf{p}}=(\overline{p}_1,\cdots,\overline{p}_\Gamma)$ is the sparse source power. When $\overline{\theta}_i$ is the true direction of the arrival, that is, $\overline{\theta}_i=\theta_i$, then $\overline{p}_i=\sigma_i^2$ and $\overline{p}_i=0$ except for the true direction of the arrival. Construct optimization cost function based on this sparse model:

$$\begin{aligned} \min_{\overline{\mathbf{p}}}\quad & \|\overline{\mathbf{p}}\|_0 \\ \text{s.t.}\quad & \left\|\mathbf{z}-\widetilde{\mathbf{B}}\left(\overline{\theta}_1,\overline{\theta}_2,\cdots\overline{\theta}_\Gamma\right)\overline{\mathbf{p}}-\sigma_n^2\widetilde{\mathbf{I}}\right\|<\varepsilon \end{aligned} \tag{24}$$

ε is positive and small enough. Unconstrained transformation and convex transformation are applied to the preceding expression, and the following expressions are obtained:

$$\widehat{\mathbf{p}}=\min_{\overline{\mathbf{p}}}\frac{1}{2}\left\|\mathbf{z}-\widetilde{\mathbf{B}}\left(\overline{\theta}_1,\overline{\theta}_2,\cdots\overline{\theta}_\Gamma\right)\overline{\mathbf{p}}\right\|_2+\eta\|\overline{\mathbf{p}}\|_1 \tag{25}$$

According to the convex optimization knowledge, the sparse source power vector $\widehat{\mathbf{p}}$ can be obtained, and the angles in the redundant dictionary corresponding to the nonzero elements of the sparse signal power vector are DOAs.

5. Performance Analysis and Simulation Experiments

5.1. Cramer-Rao Lower Bound. The Cramer-rao lower bound is the lower bound of the unbiased estimation of variance, which is used to measure the deviation of the DOAs estimation. Based on [31–33], the CRLB for SANC is given. It is assumed that the noise follows the complex Gauss distribution. According to formula (9), the probability density function of the received signal is as follows:

$$\begin{aligned} \mathbf{P}\left(\mathbf{y}(1),\cdots,\mathbf{y}(K)\right)&=\frac{1}{(2\pi)^{2MK}\left(\sigma_n^2/2\right)^{2MK}} \\ &\cdot e^{-(1/\sigma^2)\sum_{k=1}^{K}[\mathbf{y}(k)-\mathbf{Bs}(k)]^{\mathrm{H}}[\mathbf{y}(k)-\mathbf{Bs}(k)]} \end{aligned} \tag{26}$$

The logarithmic likelihood function is obtained by taking the logarithm of formula (26).

$$\begin{aligned} &\mathbf{L}\left(\mathbf{y}(1),\cdots,\mathbf{y}(K)\right) \\ &\quad=-2MK\ln(2\pi)-2MK\ln\left(\frac{\sigma_n^2}{2}\right) \\ &\qquad-\frac{1}{\sigma_n^2}\sum_{k=1}^{K}\left[\mathbf{y}(k)-\mathbf{Bs}(k)\right]^{\mathrm{H}}\left[\mathbf{y}(k)-\mathbf{Bs}(k)\right] \end{aligned} \tag{27}$$

Define $\overline{\mathbf{s}}(k)=\mathrm{Re}[\mathbf{s}(k)]$, $\widetilde{\mathbf{s}}(k)=\mathrm{Im}[\mathbf{s}(k)]$, and the Fisher information matrix is $\boldsymbol{\Omega}=[E(\psi\psi^{\mathrm{T}})]^{-1}$, where

$$\psi^{\mathrm{T}}=\frac{\partial\mathbf{L}}{\partial}\left[\sigma_n^2\ \ \overline{\mathbf{s}}^{\mathrm{T}}(1)\ \ \widetilde{\mathbf{s}}^{\mathrm{T}}(1)\ \ \cdots\ \ \overline{\mathbf{s}}^{\mathrm{T}}(K)\ \ \widetilde{\mathbf{s}}^{\mathrm{T}}(K)\ \ \theta^{\mathrm{T}}\right] \tag{28}$$

The CRLB expression for the SANC configuration can be obtained from the Fisher information matrix as

$$CRLB(\theta)=\frac{\sigma_n^2}{2}\left\{\sum_{k=1}^{K}\mathrm{Re}\left[\mathbf{F}^{\mathrm{H}}(k)\,\mathbf{D}^{\mathrm{H}}\mathbf{P}_{\mathbf{B}}^{\perp}\mathbf{DF}(k)\right]\right\}^{-1} \tag{29}$$

Table 3: Simulation conditions for the experiments.

Simulation parameters	Value
Antenna number	8
Sensor locations of SANC	0, 6, 12, 15, 16, 17, 19, 20
Sensor locations of uniform array	0, 1, 2, 3, 4, 5, 6, 7
Sensor locations of nested array	0, 1, 2, 3, 4, 8, 12, 16
Sensor locations of coprime array	0, 3, 5, 6, 9, 10, 12, 15
Sensor locations of nested CADiS	0, 1, 2, 3, 8, 12, 16, 20
Sensor locations of MRA	0, 1, 2, 5, 8, 11, 12, 13
Source number	$D = 5$
DOAs	$-40^\circ, -20^\circ, 0^\circ, 20^\circ, 40^\circ$
Snapshot number	$K = 200$
Carrier frequency	$f = 2.1GHz$
Speed of light	$c = 3 \times 10^8 m/s$
Monte Carlo times	$K_m = 200$
Signal-to-noise ratio (*SNR*)	$SNR = 0 \sim 20dB$

where $\mathbf{F}(k) = \text{diag}(\mathbf{s}(k))$, $\mathbf{D} = [\partial \mathbf{B}^{\text{H}}/\partial\theta_1, \partial \mathbf{B}^{\text{H}}/\partial\theta_2, \cdots, \partial \mathbf{B}^{\text{H}}/\partial\theta_D]$, and $\mathbf{P}_{\mathbf{B}}^{\perp} = \mathbf{I} - \mathbf{P}_{\mathbf{B}} = \mathbf{I} - \mathbf{B}(\mathbf{B}^{\text{H}}\mathbf{B})^{-1}\mathbf{B}^{\text{H}}$.

5.2. Simulation Results. In order to verify the DOA estimation performance of the proposed array configuration, the simulation experiments of SANC in underdetermined condition are given. The root mean square error (RMSE) and the CRLB with the different SNRs and the different snapshots are also simulated, respectively. The compared array configurations are the typical array configurations under the same physical array sensor number, such as the uniform array, the coprime array, the nested array, the MRA array, and the CADiS array. To maximize the aperture advantages of CADiS array, the nested CADiS array is used in the simulation. The root mean square error (RMSE) represents the magnitude of the angle estimation bias, and its mathematical expression is as follows:

$$RMSE = \sqrt{\frac{1}{K_m D} \sum_{m=1}^{K_m} \sum_{i=1}^{D} \left(\widehat{\theta}_{\text{i}}(m) - \theta_i\right)^2} \tag{30}$$

where K_m is the number of Monte Carlo simulations, D is the number of source targets, and $\widehat{\theta}_i(m)$ is the ith source DOA in the mth Monte Carlo simulation. The simulation conditions are listed in Table 3.

Simulation 1. DOA estimation performance of SANC configuration in underdetermined condition.

One of the most important features of the sparse array is that it can estimate DOAs in underdetermined condition. SANC array configuration retains this advantage. To measure the DOA estimation performance of SANC in underdetermined conditions, we conducted Monte Carlo simulations with the source number of 29 and SNRs of 0dB and 20 dB. The normalized spatial spectrums for the SANC configuration are presented in Figure 5. The simulation results show that the array configuration proposed in this paper can all effectively estimate the DOAs no matter in a high SNR condition or a low SNR condition, and the higher SNR is the sharper spectrum peak is.

Simulation 2. RMSE and CRLB comparison of uniform array, coprime array, nested array, nested CADiS array, MRA array, and SANC for different SNRs.

Figure 6(a) shows the results of the RMSE and CRLB performance of the different configurations. Figure 6(b) presents the results of the RMSE of the different DOA estimation methods, including MUSIC, the spatial smoothing MUSIC (ss-MUSIC), root-MUSIC, LASSO, and the four-order cumulant (FOC) methods. The simulation results show that the proposed configuration obviously improves the DOA estimation accuracy, and the CRLB is effectively reduced. Under this SANC configuration, the estimation performances of spatial smoothing MUSIC and root-MUSIC are basically the same. The performance of the spatial smoothing MUSIC, root-MUSIC, LASSO, and MUSIC methods is higher than the four-order cumulant method.

Simulation 3. RMSE comparison of uniform array, coprime array, nested array, nested CADiS array, MRA array, and SANC for different snapshot numbers.

The number of snapshots is an important factor for the DOA estimation accuracy. The Monte Carlo experiments simulate the RMSE of the DOA estimations with different snapshot numbers at SNRs of 0dB and 20dB. The simulation results in Figure 7 show that as the number of snapshots increases, the RMSE decreases. For each snapshot number, the RMSE of SANC is lower than that of the other configurations no matter in a low SNR or a high SNR.

6. Conclusion

In order to solve the problem of low DOF and smaller continuous virtual aperture in the existing sparse array for noncircular sources, a high degree of freedom sparse array design method suitable for noncircular sources is presented. The method uses the difference set to establish the virtual

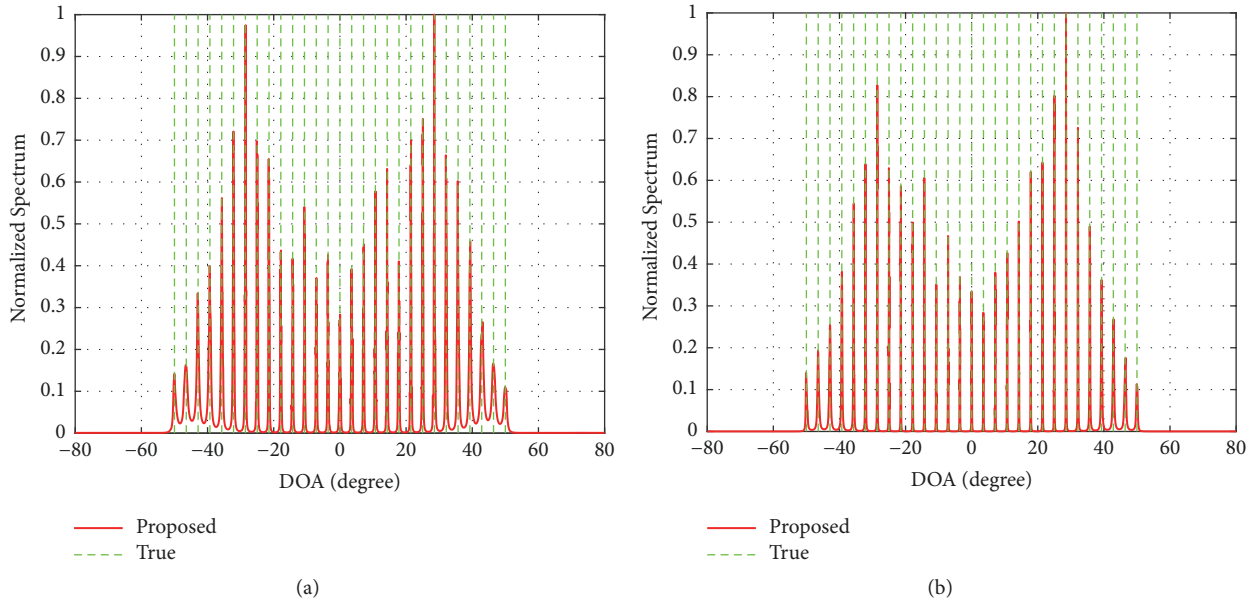

Figure 5: Normalized spatial spectrum results for a source number of 29: (a) SNR = 0dB; (b) SNR = 20dB.

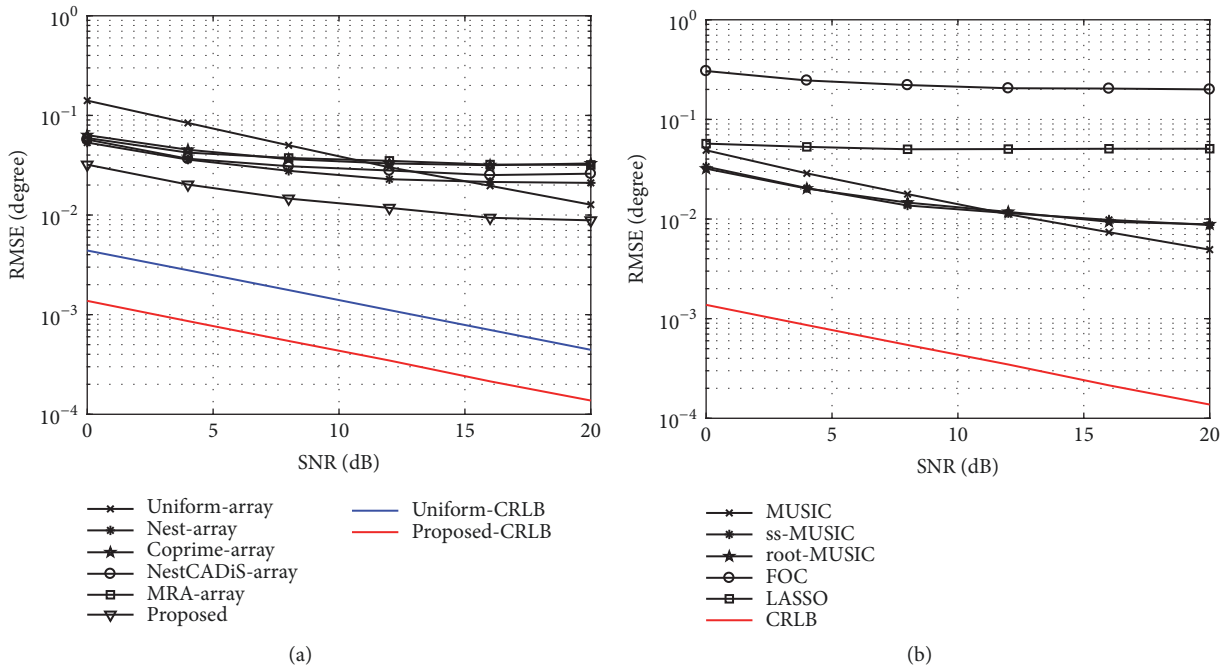

Figure 6: DOA estimation comparison under different SNRs: (a) RMSE for different array configurations. (b) RMSE for different DOA estimation methods.

array model and then expands the virtual array aperture with the characteristic of noncircular sources. The physical sensors distribution of the maximum continuous virtual array length is given by searching method. SANC gives the optimal array design for noncircular sources, and the comparisons and analysis between the proposed array configuration and the typical array configurations are also given. The simulation experiments show that, compared with the uniform array, the coprime array, the nested array, the MRA array, and the CADiS array under the same physical sensor number, the sparse array proposed for noncircular sources is significantly improved in the array aperture, array DOF, and estimation precision.

Data Availability

The authors claim that the data used in this article are provided by their simulations and this is developed without

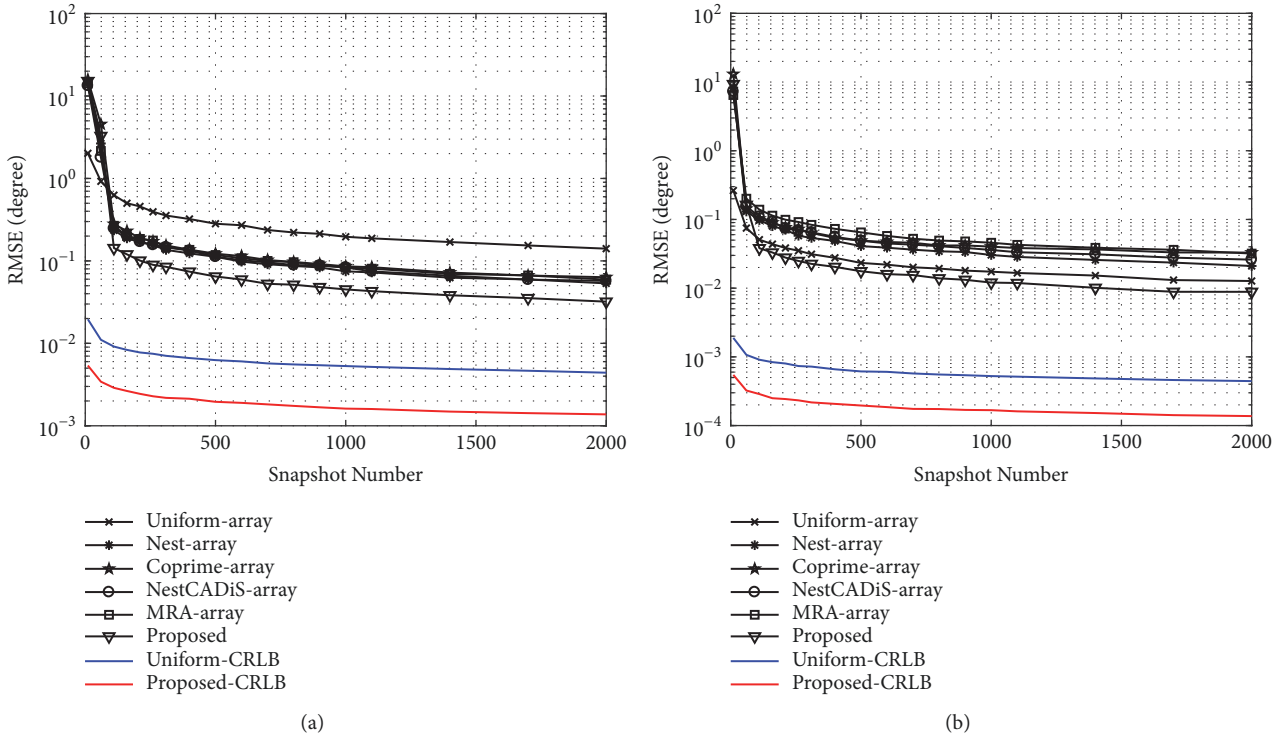

Figure 7: RMSE performance for different snapshot numbers: (a) SNR of 0dB; (b) SNR of 20dB.

using any data in a published article to support their results.

Conflicts of Interest

The authors confirm that the funding did not lead to any conflicts of interests regarding the publication of this manuscript.

Acknowledgments

The work is supported by the National Natural Science Foundation of China (Grant no. 61401513).

References

[1] Y. Qin, Y. Liu, J. Liu, and Z. Yu, "Underdetermined wideband DOA estimation for off-grid sources with coprime array using Sparse Bayesian learning," *Sensors*, vol. 18, no. 1, pp. 253–263, 2018.

[2] W. Wang, S. Ren, and Z. Chen, "Unified coprime array with multi-period subarrays for direction-of-arrival estimation," *Digital Signal Processing*, vol. 74, pp. 30–42, 2018.

[3] K. Liu and Y. D. Zhang, "Coprime array-based DOA estimation in unknown nonuniform noise environment," *Digital Signal Processing*, vol. 79, pp. 66–74, 2018.

[4] Z. Shi, C. Zhou, Y. Gu, N. A. Goodman, and F. Qu, "Source estimation using coprime array: A sparse reconstruction perspective," *IEEE Sensors Journal*, vol. 17, no. 3, pp. 755–765, 2017.

[5] C. Zhou and J. Zhou, "Direction-of-arrival estimation with coarray ESPRIT for coprime array," *Sensors*, vol. 17, no. 8, pp. 1779–1795, 2017.

[6] J. Li, D. Li, D. Jiang, and X. Zhang, "Extended-aperture unitary root music-based doa estimation for coprime array," *IEEE Communications Letters*, vol. 22, no. 4, pp. 752–755, 2018.

[7] C.-L. Liu and P. P. Vaidyanathan, "Cramér–Rao bounds for coprime and other sparse arrays, which find more sources than sensors," *Digital Signal Processing*, vol. 61, pp. 43–61, 2017.

[8] M. Ishiguro, "Minimum redundancy linear arrays for a large number of antennas," *Radio Science*, vol. 15, no. 6, pp. 1163–1170, 1980.

[9] J. P. Robinson, "Genetic search for Golomb arrays," *IEEE Transactions on Information Theory*, vol. 46, no. 3, pp. 1170–1173, 2000.

[10] P. Pal and P. P. Vaidyanathan, "Multiple level nested array: an efficient geometry for 2*q*th order cumulant based array processing," *IEEE Transactions on Signal Processing*, vol. 60, no. 3, pp. 1253–1269, 2012.

[11] P. Pal and P. P. Vaidyanathan, "Nested arrays: a novel approach to array processing with enhanced degrees of freedom," *IEEE Transactions on Signal Processing*, vol. 58, no. 8, pp. 4167–4181, 2010.

[12] C.-L. Liu and P. P. Vaidyanathan, "Super nested arrays: linear sparse arrays with reduced mutual coupling—Part I: Fundamentals," *IEEE Transactions on Signal Processing*, vol. 64, no. 15, pp. 3997–4012, 2016.

[13] P. P. Vaidyanathan and P. Pal, "Sparse sensing with co-prime samplers and arrays," *IEEE Transactions on Signal Processing*, vol. 59, no. 2, pp. 573–586, 2011.

[14] Z. Tan, Y. C. Eldar, and A. Nehorai, "Direction of arrival estimation using co-prime arrays: a super resolution viewpoint," *IEEE Transactions on Signal Processing*, vol. 62, no. 21, pp. 5565–5576, 2014.

[15] F.-G. Yan, S. Liu, J. Wang, M. Jin, and Y. Shen, "Fast DOA estimation using co-prime array," *IEEE Electronics Letters*, vol. 54, no. 7, pp. 409-410, 2018.

[16] F. Sun, P. Lan, and B. Gao, "Partial spectral search-based DOA estimation method for co-prime linear arrays," *IEEE Electronics Letters*, vol. 51, no. 24, pp. 2053–2055, 2015.

[17] J. Liu, Y. Zhang, Y. Lu, and W. Wang, "DOA estimation based on multi-resolution difference co-array perspective," *Digital Signal Processing*, vol. 62, pp. 187–196, 2017.

[18] S. Qin, Y. D. Zhang, and M. G. Amin, "Generalized coprime array configurations for direction-of-arrival estimation," *IEEE Transactions on Signal Processing*, vol. 63, no. 6, pp. 1377–1390, 2015.

[19] Y. D. Zhang, S. Qin, and M. G. Amin, "Doa estimation exploiting coprime arrays with sparse sensor spacing," in *Proceedings of the 2014 IEEE International Conference on Acoustics, Speech, and Signal Processing, ICASSP 2014*, pp. 2267–2271, Florence, Italy, 2014.

[20] S. Ren, W. Wang, and Z. Chen, "DOA estimation exploiting unified coprime array with multi-period subarrays," in *Proceedings of the 2016 CIE International Conference on Radar, (RADAR '16)*, pp. 1–4, Guangzhou, China, 2016.

[21] S. M. Alamoudi, M. A. Aldhaheri, S. A. Alawsh, and A. H. Muqaibel, "Sparse DOA estimation based on a shifted coprime array configuration," in *Proceedings of the 16th Mediterranean Microwave Symposium, (MMS '16)*, pp. 1–4, Abu Dhabi, UAE, 2016.

[22] Z.-L. Dai, W.-J. Cui, B. Ba, and Y.-K. Zhang, "Two-dimensional direction-of-arrival estimation of coherently distributed noncircular signals via symmetric shift invariance," *Acta Physica Sinica*, vol. 66, no. 22, Article ID 220701, 2017.

[23] Z. Chen, Y. Ding, S. Ren, and Z. Chen, "A novel noncircular MUSIC algorithm based on the concept of the difference and sum coarray," *Sensors*, vol. 18, no. 2, pp. 344–360, 2018.

[24] Z. Chen, S. Ren, and W. Wang, "DOA estimation exploiting extended co-array of coprime array," in *Proceedings of the 2016 CIE International Conference on Radar, (RADAR '16)*, pp. 1–4, Belfast Waterfront Conference Centre, UK, 2016.

[25] X. Wang, Z. Chen, S. Ren, and S. Cao, "DOA estimation based on the difference and sum coarray for coprime arrays," *Digital Signal Processing*, vol. 69, pp. 22–31, 2017.

[26] H. Zhai, X. Zhang, and W. Zheng, "DOA estimation of noncircular signals for coprime linear array via locally reduced-dimensional Capon," *International Journal of Electronics*, vol. 105, no. 5, pp. 709–724, 2018.

[27] K. Shabir, Z. Ye, T. Hasan, Y. Ali, and R. Ullah, "Efficient underdetermined DOA estimation algorithm by extending covariance matrix based on non-circularity using coprime array," *Communications on Applied Electronics*, vol. 7, no. 1, pp. 1–5, 2017.

[28] M. D'Urso, G. Prisco, and R. Tumolo, "Maximally sparse, steerable, and nonsuperdirective array antennas via convex optimizations," *Institute of Electrical and Electronics Engineers. Transactions on Antennas and Propagation*, vol. 64, no. 9, pp. 3840–3849, 2016.

[29] E. J. Candès, M. B. Wakin, and S. P. Boyd, "Enhancing sparsity by reweighted *l*1 minimization," *Journal of Fourier Analysis and Applications*, vol. 14, no. 5, pp. 877–905, 2008.

[30] G. Prisco and M. D'Urso, "Maximally sparse arrays via sequential convex optimizations," *IEEE Antennas and Wireless Propagation Letters*, vol. 11, pp. 192–195, 2012.

[31] B. Ba, G.-C. Liu, T. Li, Y.-C. Lin, and Y. Wang, "Joint for time of arrival and direction of arrival estimation algorithm based on the subspace of extended hadamard product," *Acta Physica Sinica*, vol. 64, no. 7, Article ID 78403, 2015.

[32] M. Wang and A. Nehorai, "Coarrays, music, and the cramer–rao bound," *IEEE Transactions on Signal Processing*, vol. 65, no. 4, pp. 933–946, 2017.

[33] P. Stoica and A. Nehorai, "Music, maximum likelihood, and cramer-rao bound," *IEEE Transactions on Acoustics, Speech, and Signal Processing*, vol. 37, no. 5, pp. 720–741, 1989.